

1 This is a non-peer reviewed preprint submitted to EarthArXiv. It has been submitted for publication in Quaternary
2 Geochronology and has yet to be accepted for publication. Subsequent versions of this manuscript may have slightly different
3 content. If accepted, the final published version of this manuscript will be available via the "Peer-reviewed Publication DOI"
4 link. Please contact the corresponding author with any feedback.

5

6 **Accurate chronological construction for two young stalagmites from the** 7 **tropical South Pacific**

8 Mohammadali Faraji^{a,*}, Silvia Frisia^a, Quan Hua^b, Andrea Borsato^a, Monika Markowska^c

9 a. School of Environmental and Life Sciences, The University of Newcastle, NSW 2308, Australia.

10 b. Australian Nuclear Science and Technology Organisation, Locked Bag 2001, Kirrawee DC, NSW 2232,
11 Australia.

12 c. Climate Geochemistry Department, Max Planck Institute for Chemistry, 55128 Mainz, Germany.

13 *Correspondence to: M.F. (mohammadali.faraji@uon.edu.au)

14 **Abstract**

15 Modern to Holocene tropical Pacific stalagmites are commonly difficult to date with the U-series, the
16 most commonly used dating method for speleothems. When U-series does not provide robust age
17 models, due to multiple sources of ²³⁰Th or little U, radiocarbon is, potentially, the best alternative.
18 The ¹⁴C content of two stalagmites (Pu17 and Nu16) collected from Pouatea and Nurau caves in the
19 Cook Island Archipelago of the South Pacific were measured to obtain accurate chronology for their
20 most modern parts. The bomb-pulse soil continuum modelling indicates that bomb radiocarbon in
21 Pu17 onsets in 1956 and reaches its maximum in 1966 CE, suggesting a fast transfer of atmospheric
22 carbon to the stalagmite of < 1 year. The modelling for Pu17 suggests a 20% contribution from C₁ - an
23 instantaneous carbon source, which renders possible an immediate transfer of atmospheric signal into
24 the cave. Nu16 shows a slower transfer of atmospheric carbon to the stalagmite than Pu17, with bomb
25 radiocarbon onsetting in 1957 CE and peaking in 1972 CE. The less negative δ¹³C values in Nu16 than

26 Pu17, and also the modelling corroborated this, which points out no contribution from the
27 instantaneous carbon source. The radiocarbon age models and laminae counting age models were
28 then spliced to achieve a single master chronology for the top part of each stalagmite. This study is an
29 example of ^{14}C age modelling combined with visible physical and chemical laminae counting and how
30 it can improve the accuracy and precision of dating for otherwise hard-to-date tropical Pacific
31 speleothems. Such accurate and precise age models pave the way to obtain sub-annually resolved
32 paleoclimate records by further improving the calibration of climate proxy data with the current and
33 instrumental weather parameters.

34 **Keywords:** radiocarbon, chronological construction, Southern Cook Islands, speleothems, tropical
35 South Pacific.

36 1. Introduction

37 In the last couple of decades, speleothems have been used to develop terrestrial paleoclimate
38 reconstructions on a wide range of temporal resolutions from seasonal to millennial scales ([Fairchild](#)
39 [and Baker, 2012](#)). These records are now available for different climate settings (e.g. [Bar-Matthews et](#)
40 [al., 1999](#); [Li et al., 2005](#); [Vansteenberghe et al., 2020](#); [Wang et al., 2019](#)), but scarce for the South Pacific
41 islands. Additionally, the instrumental records in this region are typically short and incomplete,
42 providing only a snap-shot of the range of regional natural climate variability. The South Pacific
43 islanders are highly vulnerable to the effects of both climate variability ([Cai et al., 2015](#)) and climate
44 change ([Held and Soden, 2006](#); [Xie et al., 2010](#)). However, as [Widlansky et al. \(2012\)](#) highlighted, there
45 is significant uncertainty in how the South Pacific Convergence Zone (SPCZ), the largest rainband in
46 the Southern Hemisphere, will respond in the future under a changing climate. Therefore, there is
47 sufficient justification for developing robust, accurately dated paleoclimate reconstructions from
48 stalagmites, given that in this region, water for agriculture is almost entirely supplied by rainfall rather
49 than by irrigation systems ([Barnett, 2011](#)).

50 One of the strengths of speleothems as a paleoclimatic archive is, arguably, their capability to be
51 accurately and precisely dated via radiometric methods ([Dorale et al., 2004](#); [Harmon et al., 1977](#);
52 [Hellstrom, 2006](#); [Richards et al., 1998](#); [Scholz and Hoffmann, 2008](#); [Zhao et al., 2003](#)). The U-series
53 disequilibrium method is the most commonly used dating method for speleothems ([Hellstrom, 2003](#)).
54 In the case that U-series dating cannot be applied, for example, because of multiple sources of ²³⁰Th
55 ([Hua et al., 2012](#)), robust relative chronologies can be acquired via counting annual visible chemical
56 and physical laminae ([Baker et al., 2021](#)) on two-dimensional maps ([Faraji et al., 2021](#); [Oriani et al.,](#)
57 [2022](#)). This approach may also entail considerable uncertainties, particularly in the youngest, modern
58 parts of the speleothem due to fabric complexity maps ([Faraji et al., 2021](#)). An alternative method for
59 obtaining accurate age models and further constraining the age of modern speleothems(1950 CE –
60 present) is using the radiocarbon [¹⁴C] “bomb-pulse” method (e.g. [Genty and Massault, 1999](#); [Hodge](#)

61 [et al., 2011](#); [Hua et al., 2012](#); [Markowska et al., 2019](#); [Mattey et al., 2008](#); [Noronha et al., 2015](#);
62 [Scroton et al., 2021](#)). Calibrated radiocarbon ages can also be used as an age constraint up to ~50 ka.
63 However, its use in speleothems is complicated by the contribution of ‘radioactively dead’ carbon,
64 known as Dead Carbon Proportion (DCP), derived from ^{14}C -depleted material from bedrock and aged
65 soil organic matter. Consequently, when comparing the radiocarbon ages of speleothems to the ages
66 obtained by the U–Th method, they commonly show older ages ([Beck et al., 2001](#); [Goslar et al., 2000](#)).
67 A thorough understanding of DCP variations in a speleothem then can pave the way to generate a
68 reliable radiocarbon chronology and also gain insight into the variability of water-rock interactions
69 through time ([Bajo et al., 2017](#); [Griffiths et al., 2012](#)).

70 We studied two stalagmites (Pu17 from Pouatea cave and Nu16 from Nurau cave) retrieved from Atiu
71 Island, in the South Pacific to obtain accurate and precise chronologies, which is fundamental for
72 robust paleoclimate reconstructions. Similar to other speleothems from Pacific Island caves, which are
73 cut in reef limestone, speleothems in Atiu are expected to provide an excellent opportunity for
74 radiocarbon dating. That is because the rock burden above caves is 2 to 8 m, characterized by high
75 porosity resulting from incomplete diagenesis of a relatively young reef. This shallow cave system,
76 coupled with a limited and patchy soil cover, ensures rapid surface climate conditions transmission
77 into the cave. Except for some small pockets of red clay soil filling the bottom of joint-controlled karst
78 of colluvial origin ([Stoddart et al., 1990](#)), the surface above the cave is bare karst. Rapid transmission
79 of rain signal into the cave reduces the interaction between rainwater and bedrock, thus, minimizing
80 the contribution of bedrock-derived dead carbon, which is crucial for constructing reliable radiocarbon
81 age-depth models.

82 In this study, we develop a chronology for modern portions of the two stalagmites from Atiu Island by
83 using ^{14}C and the *bomb pulse soil continuum* method from [Markowska et al. \(2019\)](#). We then compare
84 different chronologies available for Pu17 and Nu16, including laminae counting and radiocarbon age
85 models, and discuss how they are combined to obtain accurate and precise chronologies, which pave

86 the way towards reconstructing hydroclimate variability from speleothems that are difficult to date in
87 their modern parts.

88 **2. Sample and site description**

89 The stalagmites selected for this study were retrieved from Atiu Island (7.25 km N-S and 6.3 km E-W),
90 the third-largest island in the Southern Cook Islands, located in latitude 20°S and longitude 158°10'W
91 in the South Pacific (**Fig. 1a, b**). Atiu, as described by [Stoddart et al. \(1990\)](#), is a highly eroded volcanic
92 island surrounded by a rim of elevated Cenozoic reefal limestone (i.e., the makatea - the Polynesian
93 word for “white stone” referring to the reef limestone ([Kirch, 2000](#))). The volcanic plateau of Atiu
94 reaches a maximum height of ≈72 m above sea level (asl), mainly covered with limonitic-nodule-
95 bearing red clay. Based on foraminifera fossils, a Plio-Pleistocene age was attributed to the uplifted
96 reefal limestone that once rimmed the volcanic island ([Marshall, 1930](#)).

97 The vegetation above both Nurau and Pouatea caves is thick, and soil cover is limited to patchy areas
98 where it has concentrated in dissolution pits and trenches. Alfisols, Mollisols and Inceptisols are the
99 main types of soils covering the island ([Bruce, 1983](#)). However, most of the karstified makatea is
100 barren limestone, where tree roots find their way underground through dissolution cracks and voids
101 in the absence of soil. The indigenous forest association above the caves consists of native *Elaeocarpus*
102 *tonganus* and *Hernandia moerenhoutiana*. Alien species, typically coconut palms, mark human impact
103 ([Holland and Olson, 1989](#)). Although a large number of weedy plants have become naturalized in the
104 central volcanic interiors of Atiu, alien species have generally not been able to spread into the
105 makatea.

106 **2.1. Pouatea cave and stalagmite Pu17**

107 Stalagmite Pu17 (**Fig. 2**) was actively growing when removed in March 2019 at a depth of ca. 7 m
108 beneath the surface within a gallery leading to the cave's southern dead-end ([Faraji et al., 2021](#)). Pu17
109 was fed by a relatively slow and constant drip (1 drop every 15 minutes), which resulted in its candle-

110 shaped morphology ([cf. Miorandi et al., 2010](#)). There were strong indications that the stalagmites
111 were actively growing, evidenced by the analysis of several dripwater in the cave indicating a pH of ≈ 8
112 and the measured dripwater Saturation Index for calcite (SI_{cc}) between 0.9 to 1. Additionally, we
113 observed calcite forming in situ on watch glasses placed under both relatively fast (1 drop per 11
114 seconds) and slow (1 drop per 50 seconds) drips. Stalagmite Pu17 is 53 mm long and grew over a
115 stalagmite stump, likely broken by humans, which highlights the importance of speleothems as a
116 ceremonial building material, according to Atiuan lore ([Trotter and Duff, 1974](#)). The stalagmite
117 provides an opportunity to unravel the history of Polynesian land use as well as climate variability.

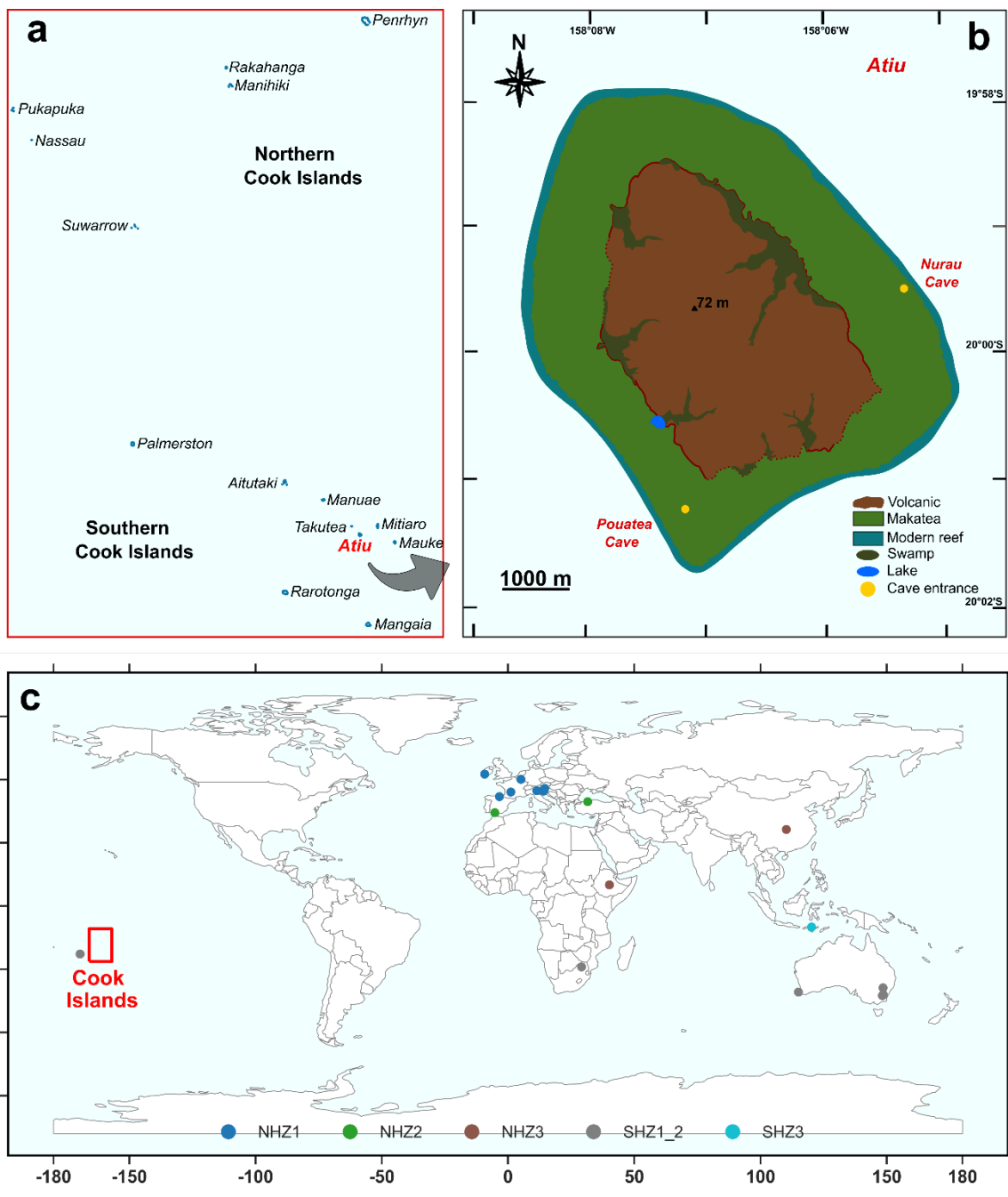
118 Pouatea cave (20°01'12"S, 158°07'10"W), located on the southwestern side of Atiu island, is a cave
119 network with several intersecting passages and side galleries with a total surveyed length of 1200 m.
120 The cave's main entrance is a vertical shaft with a drop of about 4 m that opens 23 m asl at 525 m
121 from the shoreline. There are five other entrances (skylights) with diameters ranging from 3 to 10 m
122 formed due to cave roof collapse. The rock overburden is 4 to 8 m thick, characterized by high porosity,
123 likely due to a relatively young reef's incomplete diagenesis. The porous epikarst ensures rapid
124 transmission of water through the vadose zone, further accelerated by the thin and patchy soil cover.

125 **2.2. Nurau cave and stalagmite Nu16**

126 Stalagmite Nu16 (**Fig. 2**) was retrieved from Nurau Cave in October 2018 at a depth of ca. 8 m beneath
127 the surface from a dead-end chamber. Nu16 is a 100 mm long candle-shaped stalagmite. It was
128 actively growing over a flowstone at the time of removal and was fed by a honey-coloured soda-straw
129 stalactite. The drip rate varied from 1 drop/318 seconds in the relatively dry season (measured in
130 October 2018) to 1 drop/48 seconds in the wet season (measured in March 2019). Nu16 shows clear
131 laminations throughout its growth, permitting a chronology to be constructed by counting the visible
132 laminae.

133 Nurau cave (19°59'37"S, 158°05'18"W) is located on the eastern side of Atiu island. The cave entrance,
134 which is a narrow passage at the bottom of a skylight, is 250 m from the shoreline and ca. 19 m asl.

135 Nurau was surveyed in 2018 for a total length of 500 m. Similar to other caves in Atiu, Nurau is a
 136 solution-maze cave system containing several intersecting passages and side galleries. The rock
 137 burden above the cave varies between 2 to 8 m and consists of porous reefal limestone, characterized
 138 by evidence of old palaeokarst in the form of dissolution cavities filled by calcite cement crusts.



139
 140 **Fig. 1.** a, the Northern and Southern groups of the Cook Islands (redrawn from [Australian Bureau of Meteorology and CSIRO](#)
 141 [\(2011\)](#)). b, Geomorphological map of Atiu Island (redrawn from [Stoddart et al. \(1990\)](#)) with the location of Pouatea and Nurau
 142 caves. c, location of Cook Islands and the bomb-pulse radiocarbon chronologies in the literature that was referred to in this
 143 study, the majority of which are from Northern Hemisphere Zone 1 (NHZ1). The stalagmite radiocarbon chronologies plotted
 144 in "c" are grouped according to the atmospheric ¹⁴C zones defined in [Hua et al. \(2021\)](#).

145 **3. Methods**

146 Prior to constructing radiocarbon chronologies for Pu17 and Nu16, other techniques such as U–Th
147 dating coupled with counting visible physical and chemical laminae were applied that led to
148 reasonably accurate age models. This was then followed by radiocarbon measurements and building
149 ¹⁴C age models using the soil carbon continuum modelling ([Markowska et al., 2019](#)) that enhanced the
150 accuracy of initial laminae and U-Th models. The final chronology for each stalagmite was constructed
151 by splicing the laminae counting and radiocarbon age models.

152 **3.1. Laminae counting chronology**

153 Using high-frequency variations in visible growth laminae properties ([Baker et al., 2015](#); [Tan et al.,](#)
154 [2006](#)) or the cyclicity of their geochemical properties, such as trace element concentration ([Ban et al.,](#)
155 [2018](#); [Borsato et al., 2007](#); [Jamieson et al., 2015](#); [Johnson et al., 2006](#); [Nagra et al., 2017](#); [Orland et al.,](#)
156 [2014](#); [Treble et al., 2003](#); [Wang et al., 2019](#)), or C and O isotope ratios ([Mattey et al., 2008](#); [Treble et](#)
157 [al., 2005](#)) can assist in subjugating the limitations of speleothem U–Th dating, and acquiring precise
158 relative age models. [Faraji et al. \(2021\)](#) reconstructed an age-depth model for Pu17 via integrating, in
159 a multivariate analysis, high resolution (6µm) variations in trace elements analyzed by LA-ICP-MS, with
160 optically visible growth bands and two-dimensional Sr-concentration laminae as identified through
161 synchrotron-radiation-based micro XRF (SR-µXRF) mapping. By tying the U-Th ages to the lamina
162 chronology, [Faraji et al. \(2021\)](#) reconstructed the initial ²³⁰Th/²³²Th for each U-Th sample analyzed.
163 This combined approach resulted in an age model with only 4% uncertainty, considerably improving
164 upon the ca. 50% uncertainty in the U–Th ages. Nu16, on the other hand, yielded unreliable U/Th
165 dates with age inversions, which could not be useful for age model building. However, a laminae
166 counting chronology was obtained for Nu16 via coupling SR-µXRF two-dimensional Sr-concentration
167 laminae with optical imaging of annual growth laminae. SR-µXRF microscopy that was used for
168 building laminae counting chronology was performed on polished stalagmite samples at the XFM
169 beamline at the Australian Synchrotron ([Paterson et al., 2011](#)) equipped with a Maia 384 detector

170 array mounted 10 mm away from the sample target. The beam spot size was 1.5 μm , and the
171 monochromatic incident energy was set at 18.5 keV. The XFM spectral data were analyzed using the
172 GeoPIXE software suite, quantified by using single element Mn, Fe and Pt foils (Micromatter, Canada)
173 and corrected by using a Ca matrix factor ([Borsato et al., 2021](#); [Fisher et al., 2015](#); [Ryan et al., 2010](#)).

174 However, accurate dating of the topmost parts of the two stalagmites remains disputable. That is
175 because the very recent laminations are not evident, and fabrics and growth patterns are complicated,
176 likely due to the simultaneous dissolution and precipitation of calcium carbonate. Therefore, it is
177 reasonable to examine radiocarbon as a potential dating method to build accurate chronologies for
178 the young modern parts of the Atiuan stalagmites.

179 **3.2. Radiocarbon analysis**

180 Aliquots of 8-10 mg of carbonate powders were obtained from the two stalagmites using a MicroMill
181 2002 Desktop Milling Machine equipped with tungsten carbide dental drills with a drill bit diameter of
182 1 mm, and micromilling continuously at 300 μm along the central growth axis of the stalagmite. Based
183 on the constructed lamina-based chronologies, 18 samples from the top 13 mm of Pu17 and 24
184 samples from the top 28 mm of Nu16 were then selected for AMS (accelerator mass spectrometry)
185 ^{14}C analysis. In order to minimize modern atmospheric CO_2 contamination, the sampling was carried
186 out one day before the analysis. Powdered samples were then dissolved in ~ 2 ml of 85% H_3PO_4 . Fast
187 carbonate dissolution and complete conversion to CO_2 were ensured by heating the sample vials on a
188 hot block at 90 $^\circ\text{C}$ for 1 hour. The evolved CO_2 was then converted to graphite using H_2 over Fe catalyst
189 ([Hua et al., 2001](#)). AMS measurements were carried out using the VEGA accelerator at ANSTO ([Fink et](#)
190 [al., 2004](#)) with a typical 1σ uncertainty of 0.25-0.3%. Results showing the ^{14}C content of the stalagmite
191 samples were reported as percent modern carbon (pMC ; [Stuiver and Polach, 1977](#)), after correction
192 for machine background, procedural blank, and isotopic fractionation using measured $\delta^{13}\text{C}$.

193

194 3.3. Radiocarbon age-depth modelling

195 We employed the ^{14}C bomb-pulse method to date the modern part of the Atiu's speleothems. Building
196 reliable radiocarbon chronologies for speleothems using this method, which exploits the global
197 anthropogenic increase in atmospheric ^{14}C resulting from nuclear testing in the 1950s and 1960s CE,
198 is not uncommon (e.g. [Genty and Massault, 1999](#); [Hodge et al., 2011](#); [Hua et al., 2012](#); [Markowska et](#)
199 [al., 2019](#); [Mattey et al., 2008](#); [Noronha et al., 2015](#)). The rising of the atmospheric ^{14}C concentrations
200 is around 1955 CE ([Hua et al., 2013](#); [Hua et al., 2021](#)), reaching its peak in the Northern Hemisphere
201 (NH) in 1963 CE and the Southern Hemisphere (SH) in 1965 CE. The incorporation of the elevated
202 atmospheric ^{14}C into a speleothem provides a means to determine its bomb-pulse profile. This profile
203 was established by using two main anchor points: 1) the point where ^{14}C concentrations begin to rise,
204 and 2) the date that the speleothem was retrieved from the cave (for active speleothems). However,
205 ^{14}C transferred from the atmosphere to a speleothem is typically damped and lagged due to the
206 incorporation of C from the soil organic matter above the cave, which is site-specific and has variable
207 residence times. It is, therefore, crucial to have a thorough understanding of carbon dynamics in the
208 soil zone. Several studies have modelled the age spectrum of soil organic matter to better understand
209 unsaturated zone carbon dynamics (e.g. [Carlson et al., 2019](#); [Fohlmeister et al., 2011](#); [Griffiths et al.,](#)
210 [2012](#); [Hodge et al., 2011](#); [Noronha et al., 2015](#)). Such models assume that soil gas carbon arises from
211 three different reservoirs with fast, medium and slow turnover times. The ^{14}C content recorded in a
212 speleothem is, thus, dictated by the relative C fraction in those reservoirs. These studies employ a
213 wide variety of prescribed C pool ages ranging between 1 to 10,000 years to simulate the
214 decomposition of organic C based on the humification model. One potential limitation of these models
215 is averaged or prescribed turnover time of C pools. [Markowska et al. \(2019\)](#) put forward another
216 approach that considers the decay of C as a continuum. It uses a four-reservoir model and considers
217 $^{14}\text{CO}_2$ more broadly in terms of vadose zone (root and microbial respiration) contributions. [Markowska](#)
218 [et al. \(2019\)](#)'s approach defines C pools as C_1 reservoir (turnover <1 year), bioavailable C_2 reservoir (1–
219 5 years), intermediate, chemically or physically protected C_3 reservoir (1– 40 years) and a chemically

220 or physically protected (nonbioavailable) C₄ reservoir (1–1000 years). ¹⁴C in this model is represented
221 by an array of Weibull distributions, assuming different contributions from each reservoir. The most
222 appropriate distribution is then determined using a solver function ([Markowska et al., 2019](#)), based
223 on the best fit to the speleothem ¹⁴C bomb-pulse profile, after accounting for a dead carbon
224 proportion (DCP). The DCP, which is used to account for the contribution of old carbon (from soil
225 and/or limestone bedrock), was calculated as $DCP = \left[1 - \left(\frac{{}^{14}C_{meas.}}{{}^{14}C_{atm.}} \right) \right] \times 100\%$ ([from Genty and](#)
226 [Massault, 1999](#)), where ¹⁴C_{meas.} is the measured ¹⁴C content in a speleothem and ¹⁴C_{atm.} is the ¹⁴C
227 content of the coeval atmosphere. We followed this approach to model the soil continuum for Atiu
228 caves and build robust radiocarbon chronologies for Pu17 and Nu16.

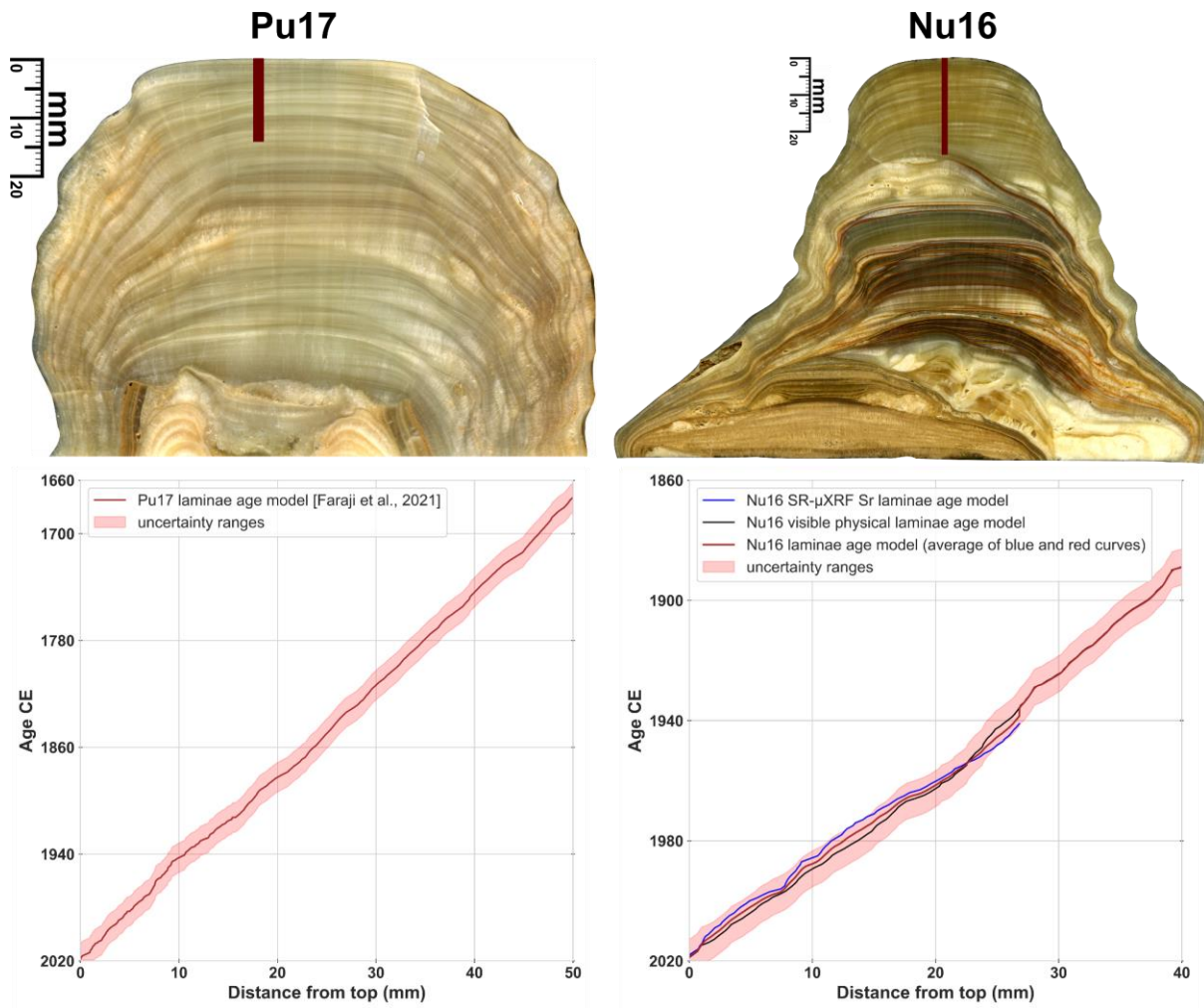
229 **3.4. Construction of final chronologies**

230 Final age models for Pu17 and Nu16 were constructed by splicing the radiocarbon and laminae age
231 models. We used the Bacon software ([Blaauw and Christen, 2011](#)), which applies a stepwise auto-
232 regressive Gamma process to generate the final chronologies. By using Bacon, the final chronology for
233 the entire Pu17, derived from the radiocarbon age model for the top 13 mm and the lamina-based
234 chronology for the whole stalagmite (50 mm), was constructed. The final age model for the top 40mm
235 of Nu16 was also achieved, based on the radiocarbon chronology for the top 28 mm and the laminae-
236 counting age model for the growth interval of 0-40 mm.

237 **4. Results**

238 The lamina-based chronology of Pu17 was discussed in [Faraji et al. \(2021\)](#) and is shown in **Fig. 2**.
239 Following the same methodology, we constructed a chronology for Nu16 based on lamina counting
240 (see **Fig. 2**) in the absence of LA-ICP-MS trace elements and without age constraints because U-Th age
241 uncertainties are substantially large and are not useful. The laminae chronology was built by assuming
242 the annual nature of laminae and assigning the age of retrieval to the topmost lamina, given that Nu16
243 was active when collected from the cave. The laminae age model reveals that the top 13 mm of Pu17,

244 where radiocarbon analysis was also conducted, grew for 92 years from 1927 to 2019 CE (Faraji et al.,
 245 2021) with a mean growth rate of $132 \pm 14 \mu\text{m}/\text{year}$. The top 28 mm of Nu16 grew for 76 years from
 246 1942 to 2018 CE with a mean growth rate of $313 \pm 39 \mu\text{m}/\text{year}$. No apparent growth interruptions
 247 were detected for neither Pu17 nor Nu16.



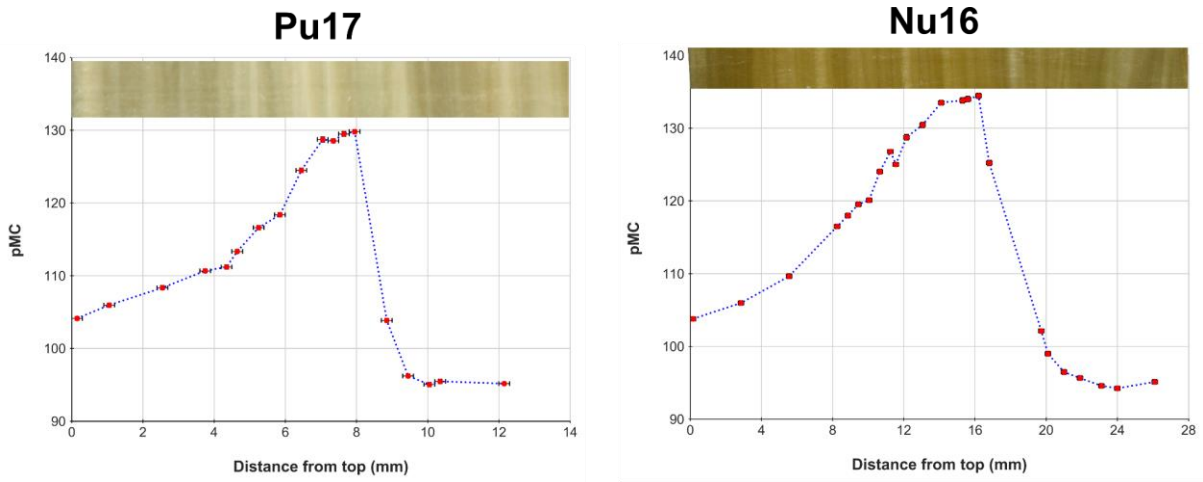
248

249 **Fig. 2.** Stalagmites Pu17 and Nu16, and their laminae counting chronologies. The red bars on the speleothem scans (top
 250 panels) show the portions analyzed for ¹⁴C.

251 The AMS ¹⁴C results are listed in **Table 1** and illustrated in **Fig. 3**. The ¹⁴C content in Pu17 is ≈ 95 pMC
 252 at a depth (distance from the top; DFT) of 12.15 mm, then slightly increases to ≈ 96 pMC at a DFT of
 253 9.45 mm. The pMC continues rising until it reaches a maximum value of ≈ 130 pMC at 7.95 mm DFT.
 254 The ¹⁴C content then fluctuates from 128-129 pMC between 7.65 and 7.05 mm DFT, after which it
 255 starts decreasing, to a value of ≈ 104 pMC at the top of Pu17. For Nu16, its ¹⁴C content is ≈ 95 pMC at
 256 26.1 mm DFT. The pMC varies around 94-95 between 26 and 21.9 mm DFT, then begins to rise at 21

257 mm, and reaches a maximum value of ≈ 134 at 16.2 mm DFT. The ^{14}C content then fluctuates around
258 133-134 pMC between 15.6 and 14 mm and declines to ≈ 103 pMC at the top of the stalagmite.

259



260

261 **Fig. 3.** The ^{14}C content in pMC (percent Modern Carbon) of the samples taken from Pu17 and Nu16 (bottom panels), and the
262 speleothem scans of the portions analyzed for ^{14}C (top panels).

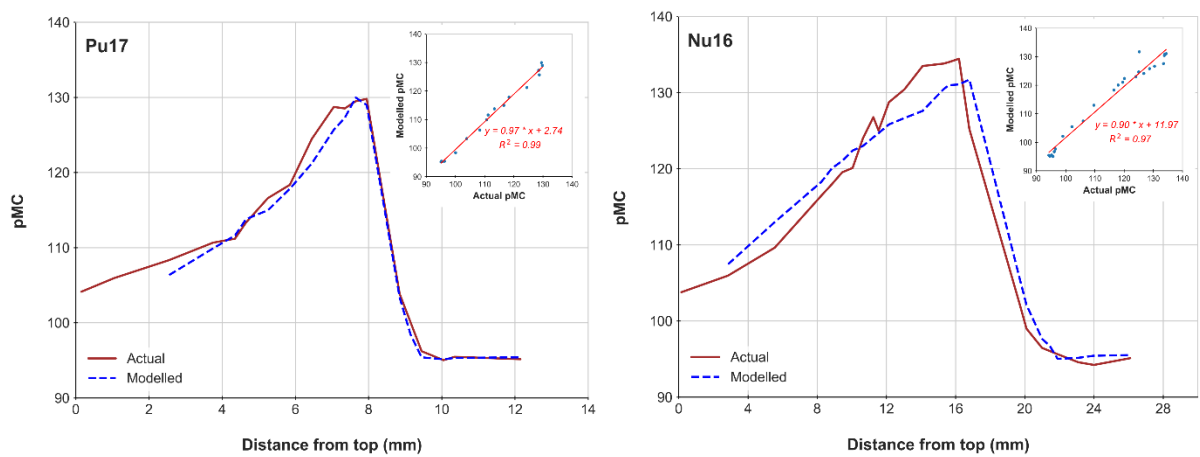
263

Lab ID (ANSTO Code)	Sample ID	DFT (mm)	¹⁴ C ± 1σ (pMC)	δ ¹³ C (‰ VPDB)
Pu17				
OZZ139	Pu17- 1	0.15	104.14 ± 0.26	-11.8
OZZ140	Pu17- 2	1.05	105.96 ± 0.28	-11.7
OZZ141	Pu17- 3	2.55	108.34 ± 0.30	-12.7
OZZ142	Pu17- 4	3.75	110.66 ± 0.26	-11.8
OZZ143	Pu17- 5	4.35	111.19 ± 0.27	-14.8
OZZ144	Pu17- 6	4.65	113.34 ± 0.28	-14.4
OZZ145	Pu17- 7	5.25	116.59 ± 0.28	-13.3
OZZ146	Pu17- 8	5.85	118.36 ± 0.28	-14.2
OZZ147	Pu17- 9	6.45	124.42 ± 0.30	-12.6
OZZ148	Pu17- 10	7.05	128.72 ± 0.34	-12.9
OZZ149	Pu17- 11	7.35	128.52 ± 0.28	-13.5
OZZ150	Pu17- 12	7.65	129.47 ± 0.32	-13.2
OZZ151	Pu17- 13	7.95	129.79 ± 0.28	-13.5
OZZ152	Pu17- 14	8.85	103.85 ± 0.26	-12.2
OZZ155	Pu17- 15	9.45	96.23 ± 0.25	-11.6
OZZ156	Pu17- 16	10.05	94.99 ± 0.27	-11.6
OZZ153	Pu17- 17	10.35	95.46 ± 0.29	-11.8
OZZ154	Pu17- 18	12.15	95.08 ± 0.23	-12.3
Nu16				
OZZ157	Nu16-1	0.15	103.78 ± 0.28	-12.8
OZZ158	Nu16-2	2.85	105.96 ± 0.31	-9.0
OZZ159	Nu16-3	5.55	109.63 ± 0.32	-8.7
OZZ160	Nu16-4	8.25	116.48 ± 0.30	-8.1
OZZ161	Nu16-5	8.85	117.96 ± 0.31	-11.1
OZZ162	Nu16-6	9.45	119.53 ± 0.31	-11.1
OZZ163	Nu16-7	10.05	120.10 ± 0.31	-9.1
OZZ164	Nu16-8	10.65	124.01 ± 0.31	-11.0
OZZ165	Nu16-9	11.25	126.77 ± 0.26	-12.4
OZZ166	Nu16-10	11.55	125.00 ± 0.26	-8.6
OZZ167	Nu16-11	12.15	128.73 ± 0.37	-10.0
OZZ168	Nu16-12	13.05	130.43 ± 0.35	-8.6
OZZ844	Nu16-13	14.10	133.49 ± 0.31	-9.1
OZZ845	Nu16-14	15.30	133.80 ± 0.37	-11.1
OZZ849	Nu16-15	15.60	133.99 ± 0.36	-10.9
OZZ846	Nu16-16	16.20	134.44 ± 0.36	-11.0
OZZ847	Nu16-17	16.80	125.20 ± 0.35	-9.5
OZZ848	Nu16-18	19.72	102.12 ± 0.28	-10.1
OZY391	Nu16-19	20.10	99.00 ± 0.32	-9.8
OZY392	Nu16-20	21.00	96.47 ± 0.32	-9.1
OZY393	Nu16-21	21.90	95.64 ± 0.31	-9.3
OZY394	Nu16-22	23.10	94.54 ± 0.31	-9.3
OZY395	Nu16-23	24.00	94.23 ± 0.30	-10.1
OZY396	Nu16-24	26.10	95.12 ± 0.30	-9.1

265 Chronological anchor points must first be assigned to build an age-depth model for Pu17 using the
266 bomb pulse soil continuum method method ([Markowska et al., 2019](#)). The first anchor point is based
267 on the 'inflection point' (IP), calculated as the mean pMC of two radiocarbon samples, the ^{14}C sample
268 where ^{14}C first appears to rise off the baseline and the closest baseline measurement. There were two
269 possibilities for the choice of the IP, either from samples Pu17-14 and -15 (DFT 9.15 mm) or from Pu17-
270 16 and -17 (DFT 9.75 mm), where we observed pMC values rising above the baseline values and hence
271 the onset of bomb radiocarbon being incorporated in the speleothem. The second anchor point used
272 was the extraction date as Pu17 was active when retrieved ([Faraji et al., 2021](#)). The age of 2019 CE
273 was assigned to the top of the stalagmite. The date of retrieval and the IP were used as anchor points
274 for the age-depth modelling. The correlation (r^2) between the modelled data and the measured data
275 (actual) was highest for the age model IP = 9.15 mm, using 1956 CE as the IP year ($r^2 = 0.99$) (**Fig. 4**).
276 This suggests a rapid transfer of the atmospheric ^{14}C to the stalagmite calcite in less than one year,
277 given the onset of atmospheric bomb radiocarbon in the SH was in early 1956 (Hua et al., 2013). The
278 age model indicates the bomb peak recorded in sample Pu-17-13 had an age of 1966 CE, also
279 suggesting negligible time delay in the transfer of atmospheric ^{14}C signal to the stalagmite as
280 atmospheric ^{14}C bomb peak in the SH occurred in 1965 CE (**Fig. 5**). Moreover, the carbon modelling
281 indicates that 20% of the C reservoir comes from an instantaneous source, labelled C_1 in **Table 2**. It is,
282 therefore, reasonable to infer an exceptionally fast transfer of atmospheric ^{14}C to Pu17. The age-depth
283 model obtained through the radiocarbon yields a growth rate of $144 \pm 8 \mu\text{m}/\text{year}$ for the top of 13mm
284 of Pu17.

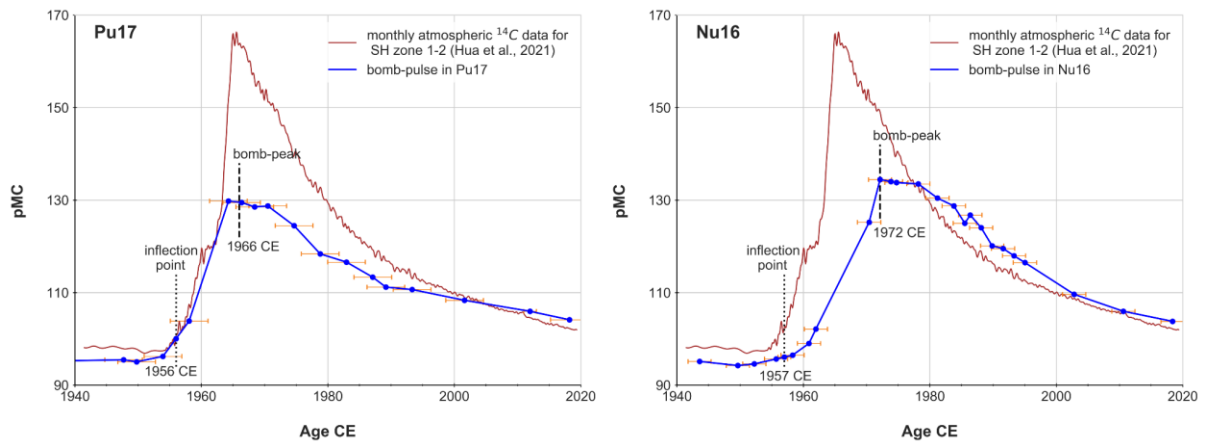
285 For Nu16, the IP was determined to be between samples Nu16-20 and 21 (DFT 21.45 mm). The r^2 value
286 between the modelled and actual data was 0.97, using 1957 CE as the IP year (onset of the bomb
287 pulse) (**Fig. 4**). This suggests that there is a slower transfer of the atmospheric carbon signal to Nu16
288 than that for Pu17. Stalagmite Nu16 was retrieved from the cave in 2018 and was still active. Thus,
289 the age of the stalagmite tip (2018 CE) and the IP were anchor points for age modelling. The Nu16
290 bomb pulse peak occurs in 1972 CE, within the sample Nu16-16 (**Fig. 5**). The modelling suggests

291 contributions predominately from C₂ and C₃, with no contribution from C₁ or C₄ (**Table 2**). Having no
 292 contribution from a C₁ reservoir also supports that Nu16 may have a slower transfer of atmospheric
 293 carbon to the stalagmite than Pu17, and consequently a later bomb peak. The less negative δ¹³C
 294 values, presented in **Table 1**, in Nu16 (mean = -10.1 ± 1.3 ‰ VPDB, n=18) compared to Pu17 (mean =
 295 -12.8 ± 0.9 ‰ VPDB, n=24) could be indicative of longer water-host rock interaction times and a slower
 296 transmissivity of rain signal to Nu16 compared to Pu17 (**Table 1**). The average DCP value for Nu16 of
 297 2.7% is similar to the DCP value for Pu17 (**Table 2**). The age-depth model yields a growth rate of 347 ±
 298 10 μm/year for the top 28 mm of Nu16, which is much higher than that of Pu17.
 299 As listed in **Table 2**, Pu17 has a 21% contribution from a very fast turnover C reservoir (C₁) which is
 300 consistent with the measured data showing a sharp ¹⁴C rise from the baseline and an early stalagmite
 301 bomb peak. On the other hand, Nu16 has no contribution from the instantaneous C pool, which results
 302 in a longer lag between the timing of the atmospheric bomb peak and that recorded in the stalagmite.
 303 Very low DCP values for both Pu17 and Nu16 account for the relatively high bomb peak values (ca.
 304 130 and 134 pMC for Pu17 and Nu16, respectively) (see **Fig. 5**), which allows reconstructing accurate
 305 radiocarbon chronologies for these two stalagmites.



306

307 **Fig. 4.** Age-depth modelling for Pu17 and Nu16 using bomb pulse soil continuum method from [Markowska et al. \(2019\)](#).
 308 Brown curves show the actual (measured) ¹⁴C data, and blue dashed curves are modelled ¹⁴C data. The correlation (*r*²)
 309 between actual and modelled data is 0.99 for Pu17 and 0.97 for Nu16 (see insert diagrams).



310

311 **Fig. 5.** Bomb pulse modelling for Pu17 and Nu16. Brown curves show monthly atmospheric ¹⁴C data for the Southern
 312 Hemisphere Zone 1-2 (Hua et al., 2021), and blue curves show the modelled ages for these stalagmites. The onset (inflection
 313 point) and the peak of the bomb pulse recorded in the stalagmites are shown. Pu17 shows a sharp and early bomb peak in
 314 1966 CE, whereas Nu16 depicts a later bomb peak in 1972 CE, indicating a slower transfer of atmospheric radiocarbon to the
 315 stalagmite.

316

317 **Table 2.** Model output from C modelling shows the contributions (%) from each C reservoir and average DCP values.

Speleothem	Modelled contribution (%) from each C reservoir				Average DCP (%) ± 1SD
	F(C ₁)	F(C ₂)	F(C ₃)	F(C ₄)	
Pu17	21	33	13	32	2.11 ± 0.47
Nu16	0	57	43	0	2.71 ± 0.55

318

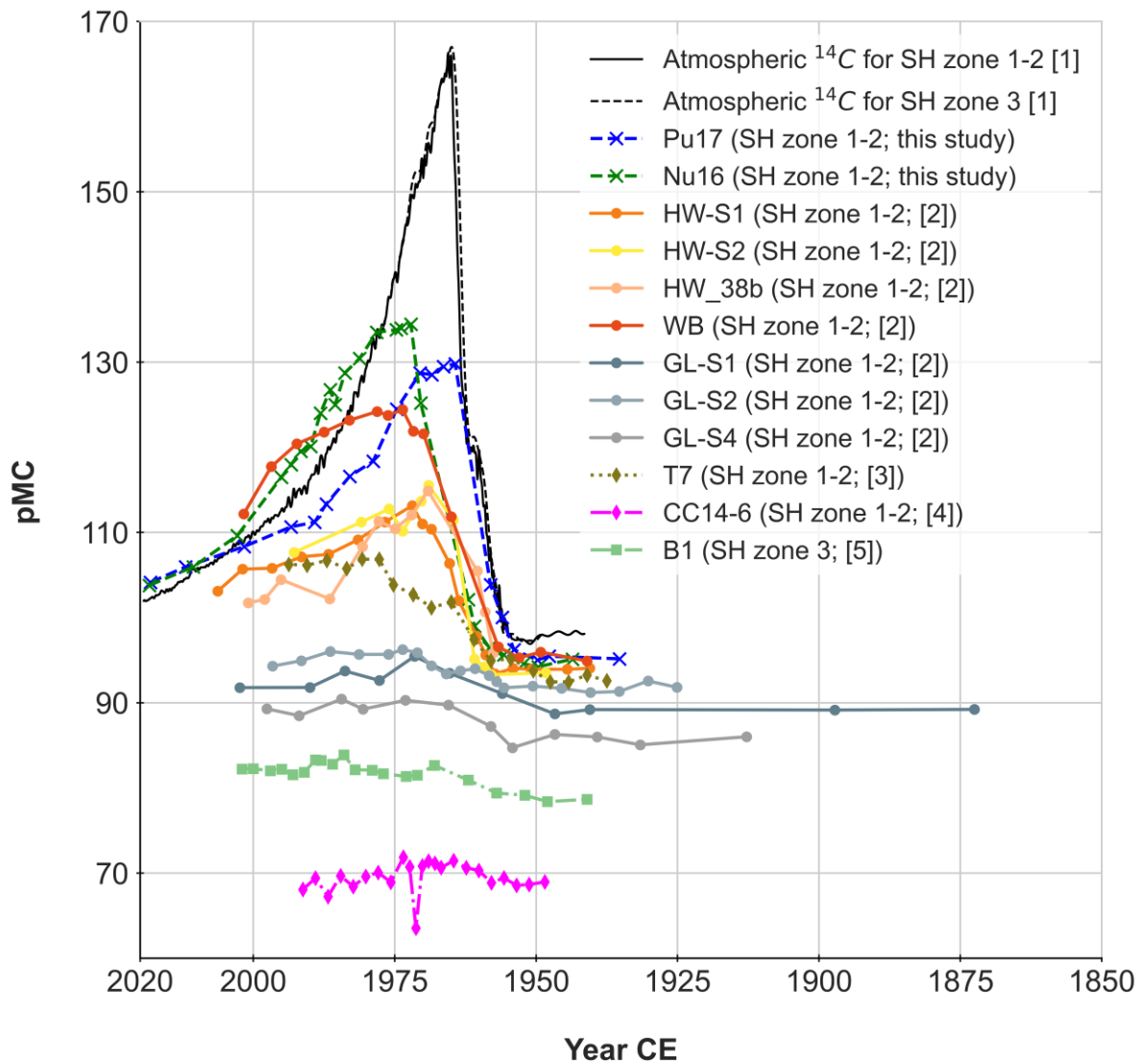
319

320 5. Discussion

321 5.1. Comparison between the bomb curves reported in this study and those in the literature

322 Comparing the radiocarbon age models of Pu17 and Nu16 with other published radiocarbon
 323 chronologies for stalagmites in the SH and the South Pacific show that Pu17 has the earliest bomb
 324 peak. In addition, both Pu17 and Nu16 record sharp rises in ¹⁴C after the bomb onsets with clearly
 325 defined bomb peaks (Fig. 6). Nu16 shows the highest peak pMC value (134.4) recorded in modern SH
 326 speleothems, being slightly higher than that in stalagmite WM4 (134.1) from the Wombeyan Caves
 327 (Hodge et al., 2011). This is likely due to the minimal overburden (2-8 m) and the sparse soil cover in

328 Atiu that in some areas, only tree litter is present. The most similar bomb-pulse radiocarbon curve to
329 Pu17 and Nu16 was reported from semi-arid Wellington Caves in southeast Australia (stalagmite WB;
330 [Markowska et al. \(2019\)](#)), where the overburden is 25 m but has limited soil cover and exposed
331 bedrock (less than 0.3 m). Bomb-pulse curves recorded in speleothems from Liang Luar cave in
332 Indonesia ([Griffiths et al., 2012](#)), Cold Air cave in South Africa ([Sundqvist et al., 2013](#)) and Careys Cave
333 in Australia ([Scropton et al., 2021](#)) are very different from those from Atiu with much-damped bomb
334 ^{14}C rising and much lower bomb peak values (**Fig. 6**). That is likely related to the site-specific soil and
335 host rock; since Liang Luar cave is buried under a thick rock burden (30-50 m) and soil cover (1-2 m),
336 the bomb peak recorded in stalagmite B1 of this cave is not clear as that reported for stalagmite T7 of
337 the Cold Air cave with a 20 m thick overburden and less than 0.3 m soil. Similarly, Careys Cave has an
338 overburden of 30 m and a very damped bomb ^{14}C . Therefore, the sharp and clear ^{14}C in the Atiuan
339 stalagmites provide excellent age models, paving the way to construct annual records of hydroclimate.



340

341 **Fig. 6.** Some of the published bomb radiocarbon chronologies for speleothems in the SH compared with those recorded in
 342 Pu17 and Nu16, and SH atmospheric ^{14}C data. [1] - [Hua et al. \(2021\)](#), [2] - [Markowska et al. \(2019\)](#), [3] - [Sundqvist et al.](#)
 343 [\(2013\)](#), [4] - [Scropton et al. \(2021\)](#), and [5] - [Griffiths et al. \(2012\)](#).

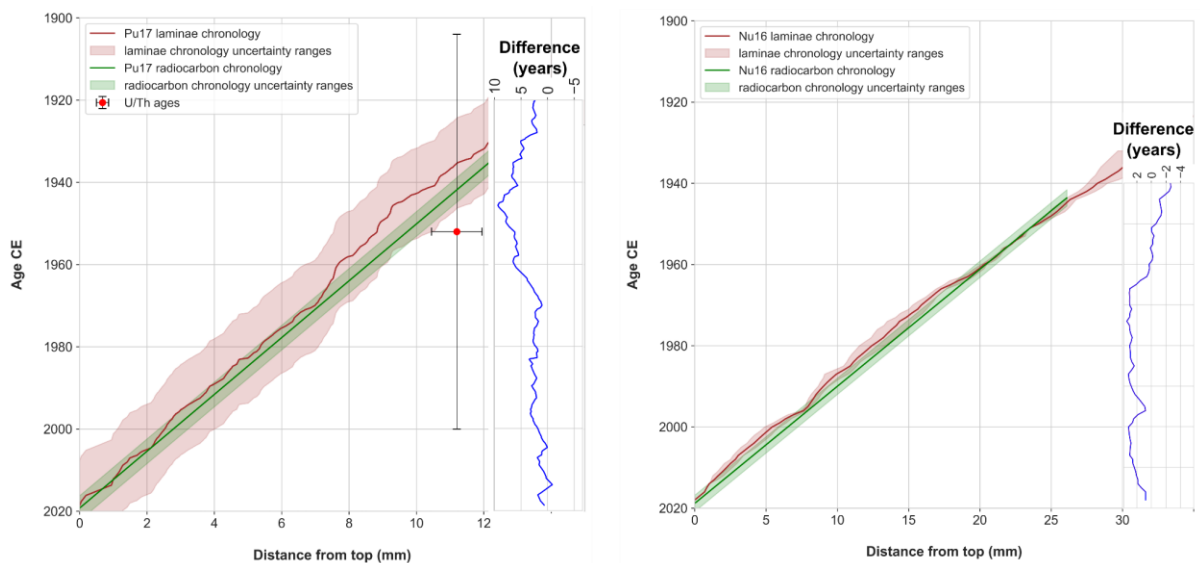
344

345 5.2. Radiocarbon vs laminae chronologies, and the final chronologies

346 Chronologies based on counting physical and chemical laminae indicate that the top 13 mm of Pu17
 347 grew for 92 years from 1927 to 2019 CE ([Faraji et al., 2021](#)), and the top 28 mm of Nu16 grew for 76
 348 years from 1942 to 2018 CE. These suggest a mean growth rate of $132 \pm 14 \mu\text{m}/\text{year}$ for Pu17 and 313
 349 $\pm 39 \mu\text{m}/\text{year}$ for Nu16. The radiocarbon chronologies indicate slightly different growth rates for the

350 top 13 mm of Pu17 (89 ± 3 years; 146 ± 5 $\mu\text{m}/\text{year}$) and the top 28 mm of Nu16 (78 ± 2 years; 358 ± 8
351 $\mu\text{m}/\text{year}$).

352 The age-depth relationship generated by radiocarbon modelling follows a constant annual growth
353 for Pu17 and Nu16, while those obtained by laminae counting show variable annual growth rates. This
354 explains why the laminae counting chronologies and those obtained through radiocarbon modelling
355 are not the same. As shown in **Fig. 7**, whilst the 1σ uncertainty ranges of laminae counting age models
356 encompass those associated with the bomb-pulse models, the difference between the two
357 approaches can be up to nine years for Pu17 and three years for Nu16 within the growth interval.
358 Interestingly, the laminae age models almost always overestimated the age of the stalagmites for at
359 least 2-3 years (**Fig. 7**). However, for most of the growth interval, the offset between the chronologies
360 is around 2-3 years for both stalagmites, which falls within the 1σ uncertainty ranges of the age models
361 (**Fig. 7**).



362

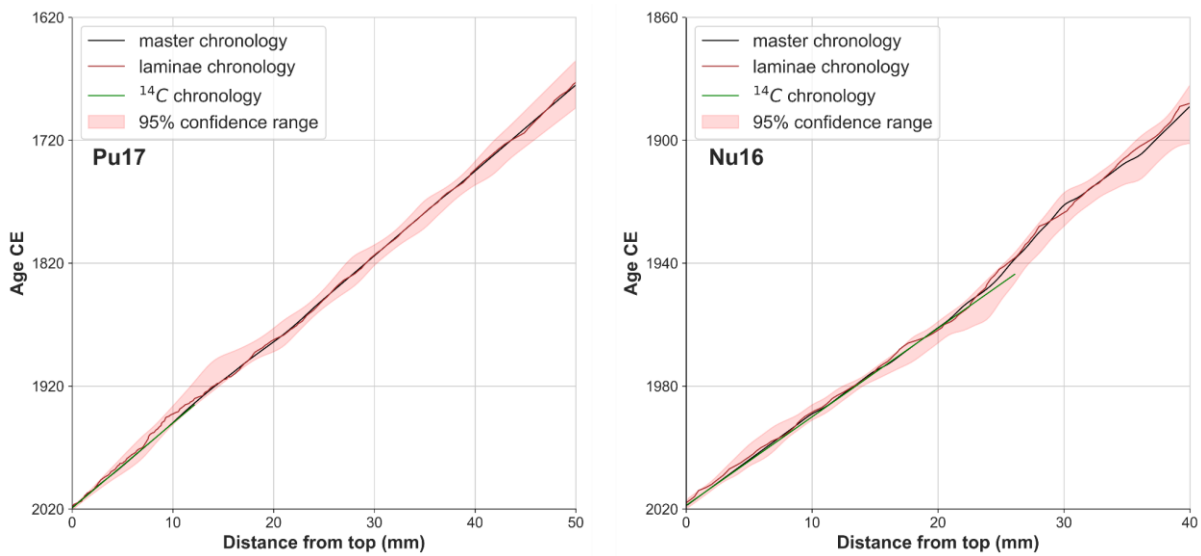
363 **Fig. 7.** Comparison of the laminae counting chronology constructed for Pu17 (Faraji et al., 2021) and Nu16 with corresponding
364 radiocarbon chronologies. The offset between the laminae and radiocarbon age models (blue curve) is mostly around 2-3
365 years, which falls within the age models' 1σ uncertainty ranges.

366

367 In order to construct the final chronologies for the entire growth interval of Pu17 (50 mm) and the top
368 40 mm of Nu16, the radiocarbon and laminae chronologies were spliced for each stalagmite. For the

369 top parts of the stalagmites where the radiocarbon and laminae age models overlap, the final
 370 chronologies are closer to the radiocarbon age model than to the laminae counting because
 371 radiocarbon has smaller uncertainties than the initial laminae age model both in Pu17 (± 3 vs ± 11 years)
 372 and Nu16 (± 2 vs ± 6 years). **Fig. 8** shows the final chronologies constructed for Pu17 and Nu16. As
 373 shown in the figure, the top 13 mm of Pu17 and top 28 mm of Nu16, where radiocarbon samples were
 374 collected, have narrower ranges of age uncertainties compared to the deeper parts. According to the
 375 final chronologies, stalagmite Pu17 grew for 347 years from 1672 to 2019 CE with an average growth
 376 rate of $144 \pm 5 \mu\text{m}/\text{year}$, and the top 40 mm of stalagmite Nu16 grew for 130 years from 1888 to 2018
 377 CE with a mean growth rate of $307 \pm 13 \mu\text{m}/\text{year}$.

378



379

380 **Fig. 8.** The final constructed chronologies (black curve) for Pu17 and Nu16 after splicing the radiocarbon (green curve) and
 381 laminae age models (brown curve) by using the Bacon age-depth modelling (Blaauw and Christen, 2011). The 95%
 382 confidence ranges were produced by Bacon and are shown in red envelopes.

383

384

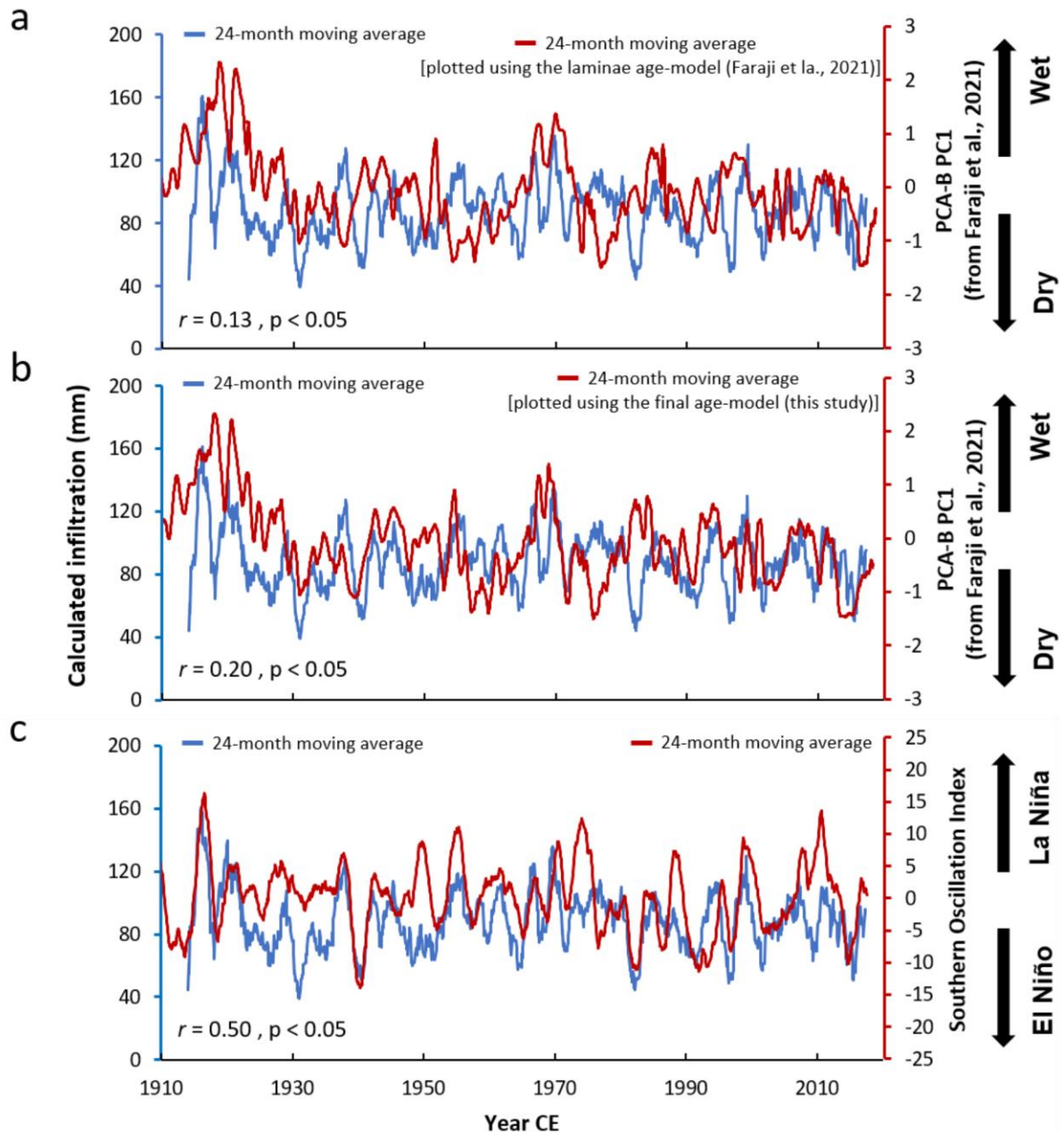
385

386

387 5.3. Implications for regional hydroclimate

388 In order to demonstrate the significance of the chronologies constructed via combining the
389 radiocarbon dating with laminae counting, we use the Pu17 hydroclimate proxies which were initially
390 discussed in [Faraji et al. \(2021\)](#). By analyzing a group of trace elements including Mg, Na, Sr, Ba through
391 LA-ICP-MS, and then performing a principal component analysis (PCA), [Faraji et al. \(2021\)](#) argued that
392 infiltration - rainfall minus potential evapotranspiration (PET) - is the mechanism controlling the
393 concentration of trace elements in Pu17. They used the Thornthwaite formula ([Thornthwaite, 1948](#))
394 to calculate the PET for Atiu for 1914-2019. The calculated infiltration was then acquired by
395 subtracting the PET from instrumental rainfall data. [Faraji et al. \(2021\)](#) showed that principal
396 component one (PC1) of the PCA, including Mg, Na, Sr, Ba that accounts for 42% variance in the trace
397 elements, correlates positively with infiltration (and thus rainfall). As such, the more positive values
398 of PC1 should correspond to higher infiltration, whilst its negative values should coincide with lower
399 infiltration. In **Fig. 9**, the PC1 is compared with the calculated infiltration in Atiu by using both the
400 laminae chronology (**Fig. 9a**) and the final chronology constructed in this study (**Fig. 9b**). In both cases,
401 PC1 follows the variation in infiltration and more positive values of PC1 point to higher infiltration.
402 However, when PC1 was plotted using the final age model developed in this study, it showed a much
403 clear relationship with infiltration with a higher correlation coefficient ($r = 0.20$) than when plotted
404 using the laminae age model ($r = 0.13$). This corroborates the idea that infiltration is the overarching
405 mechanism controlling the variability of trace elements in Pu17, even though each element might
406 originate from a different source [Faraji et al. \(2021\)](#). This also reveals the excellent potential of
407 speleothems from the Cook Islands to provide reliable information, at least, on the historical variability
408 of the El Niño Southern Oscillation (ENSO). That is because the ENSO, represented by Southern
409 Oscillation Index (SOI) in **Fig. 9c**, drives much of the interannual variation in rainfall (and thus
410 infiltration) in the Pacific Islands ([Weir et al., 2021](#)). El Niño events are generally associated with
411 relatively dry periods and less rainfall in the southern Cook Islands, whereas La Niña events mark wet
412 periods (see **Fig. 9c**). Precisely-dated high-resolution proxies of infiltration - for example, PC1 in Pu17

413 - are excellent material for reconstructing infiltration over the past, at least a few hundred years, that
 414 can cast some light on the past variation of rainfall driven by ENSO. This becomes even more important
 415 in the Pacific Islands region, where water for agriculture is almost entirely supplied by rainfall rather
 416 than by irrigation systems (Barnett, 2011).



417

418 **Fig. 9.** The laminae age model (a) and the final chronology constructed in this study (b) in comparison with the PC1 - of PCA-
 419 B in Faraji et al. (2021) - as a hydroclimate proxy with the calculated infiltration. In both cases, PC1 follows the variation in
 420 infiltration, and more positive values of PC1 correspond to higher infiltration (wet) and vice versa. However, when PC1 was
 421 plotted using the age model developed in this study, it showed a far more clear relationship with infiltration (b) than when
 422 plotted using the laminae age model (a). The calculated infiltration is also plotted against the Southern Oscillation Index
 423 (representing ENSO), showing a strong link between dry (wet) periods and El Niño (La Niña) events. The instrumental record
 424 for SOI was acquired from the Australian Bureau of Meteorology website at: <http://www.bom.gov.au/>.

425 Therefore, it is clear that joint use of bomb radiocarbon and laminae counting chronologies has
426 improved the fit between the calculated infiltration and the PC1 data, paving the way towards
427 obtaining well-dated climate records from Atiuan stalagmites. The combined chronology has
428 improved the accuracy and precision of the age model in the very young parts of the stalagmites,
429 which are otherwise hard to date due to significant uncertainties of U/Th dating and also complexities
430 in the fabrics and possible occurrence of sub-annual laminae. [Faraji et al. \(2021\)](#) were able to decrease
431 the uncertainty of U/Th chronology by 45% via counting visible physical and chemical laminae.
432 However, that laminae age model still had some 4% uncertainty. The final constructed chronology
433 developed in this study further constrained the age model for Pu17 by reducing the uncertainty for
434 the top 13 mm of the stalagmite by 3%. The final chronology for Nu16 has only 2% uncertainty in the
435 top 28 mm and up to 4% at DFT 40 mm.

436 Therefore, even though speleothems from the tropical South Pacific commonly suffer from large
437 uncertainties in their U-Th dating, the use of our combined chronological approach allows us to reduce
438 dating uncertainty and examine paleoclimate records at annual resolution. That is because these
439 speleothems usually benefit from a rapid transmissivity of rainfall in shallow caves with a porous or
440 fractured host rock. Additionally, little soil cover or tree litter further facilitates transmissivity. This, in
441 an environment with seasonal contrast in precipitation (or in cave ventilation/breathing), could
442 potentially lead to the development of both physical and chemical annual laminae in speleothems.
443 Using the combined approach of ^{14}C modelling and visible and chemical laminae counting for tropical
444 Pacific examples can improve the accuracy of dating tremendously, as was shown in this study. This
445 opens up the possibility of obtaining annually resolved hydroclimate records that advances knowledge
446 about pre-instrumental hydroclimate variability in the tropical South Pacific and reduces uncertainties
447 about the magnitude, frequency and duration of past droughts and pluvials.

448

449 6. Conclusion

450 Two stalagmites from Southern Cook Islands in the tropical South Pacific were dated using the ^{14}C
451 bomb pulse soil continuum method from [Markowska et al. \(2019\)](#). Results indicate that the onset of
452 the bomb-pulse in Pu17 starts in 1956 and reaches its bomb peak in 1966 CE. The carbon modelling
453 also indicates a 20% contribution from C_1 - an instantaneous C source. These data suggest an
454 exceptionally fast transfer of atmospheric carbon to the stalagmite <1 year, which was also supported
455 by very negative $\delta^{13}\text{C}$ values in Pu17 (<-12 ‰ VPDB). The age-depth modelling for Nu16 was indicative
456 of a slower transfer of atmospheric carbon to the stalagmite than Pu17, with a bomb radiocarbon
457 onset and bomb peak in 1957 and 1972 CE, respectively. This was corroborated by less negative $\delta^{13}\text{C}$
458 values in Nu16 (-8 to -11‰) than Pu17 (-11 to -15‰), and also by the carbon modelling that points
459 out no contribution from C_1 reservoirs.

460 The low DCP values (2-3%) in both Pu17 and Nu16, leading to their high bomb peak of 130-134 pMC,
461 render such accurate radiocarbon chronologies possible. According to the radiocarbon chronologies
462 constructed in this study, the top 13 mm of Pu17 grew for 89 years (1930 – 2019 CE) with a constant
463 growth rate of 144 $\mu\text{m}/\text{year}$. The top 28 mm of Nu16 grew for 78 years (1940 – 2018 CE) with a rate
464 more than double that of Pu17, around 347 $\mu\text{m}/\text{year}$. The radiocarbon chronologies and available
465 laminae counting age models were then spliced to achieve a single master chronology for each
466 stalagmite. The final age models suggest that Pu17 grew for 347 years from 1672 to 2019 CE, and the
467 top 40 mm of the stalagmite Nu16 grew for 130 years from 1888 to 2018 CE.

468 Based on the final constructed chronology, we compared the already published Pu17 proxies of
469 hydroclimate with the calculated infiltration record in Atiu, which showed great agreement between
470 the two series. This supports the accuracy of the final age-depth model. This also attests to the great
471 potential of Pu17, and likely Nu16 as well, to advance knowledge about pre-instrumental hydroclimate
472 variability in the tropical South Pacific. This study is an example of ^{14}C age modelling combined with
473 visible physical and chemical laminae counting and how it can improve the accuracy of dating for

474 otherwise hard-to-date tropical Pacific speleothems. Such accurate and precise chronologies allow
475 obtaining robust paleoclimate records for the climate-vulnerable South Pacific Island communities
476 through enhancing the quality of the calibration of climate proxy data with the current and
477 instrumental weather parameters measured at both cave surface and interior.

478 **Declaration of competing interest statement**

479 The authors declare that they have no known competing financial interests or personal relationships
480 that could have appeared to influence the work reported in this paper.

481

482 **Acknowledgements**

483 Special thanks to the landowners, people and Island Council, and to the National Research Committee
484 of the Cook Islands for permission to explore the caves of Atiu and take samples, and to Tura Koronui
485 and George Mateariki, who introduced us to the caves in Atiu. The radiocarbon analysis was carried
486 out at ANSTO. This study was supported by the Australian Research Council Discovery Project grant
487 DP160101058. M.F. was supported by the Australian Government through an “Australian Government
488 Research Training Program Scholarship” and was also supported by The Australian Institute of Nuclear
489 Science and Engineering through a Postgraduate Research Award (award ALNSTU12486).

490

491

492

493 **References**

- 494 Bajo, P., Borsato, A., Drysdale, R., Hua, Q., Frisia, S., Zanchetta, G., Hellstrom, J., and Woodhead, J.,
 495 2017, Stalagmite carbon isotopes and dead carbon proportion (DCP) in a near-closed-system
 496 situation: An interplay between sulphuric and carbonic acid dissolution: *Geochimica et*
 497 *Cosmochimica Acta*, v. 210, p. 208-227. <https://doi.org/10.1016/j.gca.2017.04.038>
- 498 Baker, A., C. Hellstrom, J., Kelly, B. F. J., Mariethoz, G., and Trouet, V., 2015, A composite annual-
 499 resolution stalagmite record of North Atlantic climate over the last three millennia: *Scientific*
 500 *Reports*, v. 5, p. 10307. <https://doi.org/10.1038/srep10307>
- 501 Baker, A., Mariethoz, G., Comas-Bru, L., Hartmann, A., Frisia, S., Borsato, A., Treble, P. C., and Asrat,
 502 A., 2021, The Properties of Annually Laminated Stalagmites-A Global Synthesis: *Reviews of*
 503 *Geophysics*, v. 59, no. 2, p. e2020RG000722. <https://doi.org/10.1029/2020RG000722>
- 504 Ban, F., Baker, A., Marjo, C. E., Duan, W., Li, X., Han, J., Coleborn, K., Akter, R., Tan, M., and Nagra, G.,
 505 2018, An optimized chronology for a stalagmite using seasonal trace element cycles from
 506 Shihua Cave, Beijing, North China: *Scientific Reports*, v. 8, no. 1, p. 4551.
 507 <https://doi.org/10.1038/s41598-018-22839-z>
- 508 Bar-Matthews, M., Ayalon, A., Kaufman, A., and Wasserburg, G. J., 1999, The Eastern Mediterranean
 509 paleoclimate as a reflection of regional events: Soreq cave, Israel: *Earth and Planetary Science*
 510 *Letters*, v. 166, no. 1, p. 85-95. [https://doi.org/10.1016/S0012-821X\(98\)00275-1](https://doi.org/10.1016/S0012-821X(98)00275-1)
- 511 Barnett, J., 2011, Dangerous climate change in the Pacific Islands: food production and food security:
 512 *Regional Environmental Change*, v. 11, no. 1, p. 229-237. [https://doi.org/10.1007/s10113-](https://doi.org/10.1007/s10113-010-0160-2)
 513 [010-0160-2](https://doi.org/10.1007/s10113-010-0160-2)
- 514 Beck, J. W., Richards, D. A., Lawrence, R., Edwards, Silverman, B. W., Smart, P. L., Donahue, D. J.,
 515 Herrera-Osterheld, S., Burr, G. S., Calsoyas, L., Timothy, A. J., Jull, and Biddulph, D., 2001,
 516 Extremely Large Variations of Atmospheric 14C Concentration During the Last Glacial Period:
 517 *Science*, v. 292, no. 5526, p. 2453-2458. <https://doi.org/10.1126/science.1056649>
- 518 Blaauw, M., and Christen, J. A., 2011, Flexible paleoclimate age-depth models using an autoregressive
 519 gamma process: *Bayesian Analysis*, v. 6, no. 3, p. 457-474, 418. [https://doi.org/10.1214/11-](https://doi.org/10.1214/11-BA618)
 520 [BA618](https://doi.org/10.1214/11-BA618)
- 521 Borsato, A., Frisia, S., Fairchild, I. J., Somogyi, A., and Susini, J., 2007, Trace element distribution in
 522 annual stalagmite laminae mapped by micrometer-resolution X-ray fluorescence: implications
 523 for incorporation of environmentally significant species: *Geochimica et Cosmochimica Acta*, v.
 524 71, no. 6, p. 1494-1512. <https://doi.org/10.1016/j.gca.2006.12.016>
- 525 Borsato, A., Frisia, S., Howard, D., and Greig, A., 2021, A guide to synchrotron hard X-ray fluorescence
 526 mapping of annually laminated stalagmites: Sample preparation, analysis and evaluation:
 527 *Spectrochimica Acta Part B: Atomic Spectroscopy*, p. 106308.
 528 <https://doi.org/10.1016/j.sab.2021.106308>
- 529 Bruce, J. G., 1983, Patterns and classification by soil taxonomy of the soils of the southern cook islands:
 530 *Geoderma*, v. 31, no. 4, p. 301-323. [https://doi.org/10.1016/0016-7061\(83\)90043-5](https://doi.org/10.1016/0016-7061(83)90043-5)
- 531 Cai, W., Santoso, A., Wang, G., Yeh, S.-W., An, S.-I., Cobb, K. M., Collins, M., Guilyardi, E., Jin, F.-F., Kug,
 532 J.-S., Lengaigne, M., McPhaden, M. J., Takahashi, K., Timmermann, A., Vecchi, G., Watanabe,
 533 M., and Wu, L., 2015, ENSO and greenhouse warming: *Nature Climate Change*, v. 5, no. 9, p.
 534 849-859. <https://doi.org/10.1038/nclimate2743>
- 535 Carlson, P. E., Banner, J. L., Johnson, K. R., Casteel, R. C., and Breecker, D. O., 2019, Carbon cycling of
 536 subsurface organic matter recorded in speleothem 14C records: Maximizing bomb-peak
 537 model fidelity: *Geochimica et Cosmochimica Acta*, v. 246, p. 436-449.
 538 <https://doi.org/10.1016/j.gca.2018.11.035>
- 539 Dorale, J. A., Edwards, R. L., Alexander, E. C., Shen, C.-C., Richards, D. A., and Cheng, H., Uranium-Series
 540 Dating of Speleothems: Current Techniques, Limits, & Applications, Boston, MA, 2004,
 541 Springer US, p. 177-197.

542 Fairchild, I. J., and Baker, A., 2012, Speleothem science: from process to past environments, John Wiley
543 & Sons.

544 Faraji, M., Borsato, A., Frisia, S., Hellstrom, J. C., Lorrey, A., Hartland, A., Greig, A., and Matthey, D. P.,
545 2021, Accurate dating of stalagmites from low seasonal contrast tropical Pacific climate using
546 Sr 2D maps, fabrics and annual hydrological cycles: *Scientific Reports*, v. 11, no. 1, p. 2178.
547 <https://doi.org/10.1038/s41598-021-81941-x>

548 Fink, D., Hotchkis, M., Hua, Q., Jacobsen, G., Smith, A. M., Zoppi, U., Child, D., Mifsud, C., van der Gaast,
549 H., Williams, A., and Williams, M., 2004, The ANTARES AMS facility at ANSTO: *Nuclear*
550 *Instruments and Methods in Physics Research Section B: Beam Interactions with Materials and*
551 *Atoms*, v. 223-224, p. 109-115. <https://doi.org/10.1016/j.nimb.2004.04.025>

552 Fisher, L. A., Fougereuse, D., Cleverley, J. S., Ryan, C. G., Micklethwaite, S., Halfpenny, A., Hough, R.
553 M., Gee, M., Paterson, D., Howard, D. L., and Spiers, K., 2015, Quantified, multi-scale X-ray
554 fluorescence element mapping using the Maia detector array: application to mineral deposit
555 studies: *Mineralium Deposita*, v. 50, no. 6, p. 665-674. [https://doi.org/10.1007/s00126-014-](https://doi.org/10.1007/s00126-014-0562-z)
556 [0562-z](https://doi.org/10.1007/s00126-014-0562-z)

557 Fohlmeister, J., Kromer, B., and Mangini, A., 2011, The Influence of Soil Organic Matter Age Spectrum
558 on the Reconstruction of Atmospheric 14C Levels via Stalagmites, v. 53, no. 1, p. 99 - 115.
559 <https://doi.org/10.1017/s003382220003438x>

560 Genty, D., and Massault, M., 1999, Carbon transfer dynamics from bomb-14C and $\delta^{13}C$ time series of
561 a laminated stalagmite from SW France—modelling and comparison with other stalagmite
562 records: *Geochimica et Cosmochimica Acta*, v. 63, no. 10, p. 1537-1548.
563 [https://doi.org/10.1016/S0016-7037\(99\)00122-2](https://doi.org/10.1016/S0016-7037(99)00122-2)

564 Goslar, T., Hercman, H., and Pazdur, A., 2000, Comparison of U-Series and Radiocarbon Dates of
565 Speleothems, v. 42, no. 3, p. 403 - 414. <https://doi.org/10.1017/s0033822200030332>

566 Griffiths, M. L., Fohlmeister, J., Drysdale, R. N., Hua, Q., Johnson, K. R., Hellstrom, J. C., Gagan, M. K.,
567 and Zhao, J. x., 2012, Hydrological control of the dead carbon fraction in a Holocene tropical
568 speleothem: *Quaternary Geochronology*, v. 14, p. 81-93.
569 <https://doi.org/10.1016/j.quageo.2012.04.001>

570 Harmon, R. S., Ford, D. C., and Schwarcz, H. P., 1977, Interglacial chronology of the Rocky and
571 Mackenzie Mountains based upon 230Th–234U dating of calcite speleothems: *Canadian*
572 *Journal of Earth Sciences*, v. 14, no. 11, p. 2543-2552. <https://doi.org/10.1139/e77-220>

573 Held, I. M., and Soden, B. J., 2006, Robust Responses of the Hydrological Cycle to Global Warming:
574 *Journal of Climate*, v. 19, no. 21, p. 5686-5699. <https://doi.org/10.1175/jcli3990.1>

575 Hellstrom, J., 2003, Rapid and accurate U/Th dating using parallel ion-counting multi-collector ICP-MS:
576 *Journal of Analytical Atomic Spectrometry*, v. 18, no. 11, p. 1346.
577 <https://doi.org/10.1039/b308781f>

578 Hellstrom, J., 2006, U–Th dating of speleothems with high initial 230Th using stratigraphical constraint:
579 *Quaternary Geochronology*, v. 1, no. 4, p. 289-295.
580 <https://doi.org/10.1016/j.quageo.2007.01.004>

581 Hodge, E., McDonald, J., Fischer, M., Redwood, D., Hua, Q., Levchenko, V., Drysdale, R., Waring, C.,
582 and Fink, D., 2011, Using the 14C Bomb Pulse to Date Young Speleothems: *Radiocarbon*, v. 53,
583 no. 2, p. 345-357. <https://doi.org/10.1017/S0033822200056605>

584 Holland, P., and Olson, S., 1989, Introduced versus native plants in austral forests: *Progress in Physical*
585 *Geography: Earth and Environment*, v. 13, no. 2, p. 260-293.
586 <https://doi.org/10.1177/030913338901300205>

587 Hua, Q., Barbetti, M., and Rakowski, A. Z., 2013, Atmospheric Radiocarbon for the Period 1950–2010:
588 *Radiocarbon*, v. 55, no. 4, p. 2059-2072. https://doi.org/10.2458/azu_js_rc.v55i2.16177

589 Hua, Q., Jacobsen, G. E., Zoppi, U., Lawson, E. M., Williams, A. A., Smith, A. M., and McGann, M. J.,
590 2001, Progress in radiocarbon target preparation at the ANTARES AMS Centre: *Radiocarbon*,
591 v. 43, no. 2A, p. 275-282. <https://doi.org/10.1017/S003382220003811X>

592 Hua, Q., McDonald, J., Redwood, D., Drysdale, R., Lee, S., Fallon, S., and Hellstrom, J., 2012, Robust
593 chronological reconstruction for young speleothems using radiocarbon: *Quaternary*
594 *Geochronology*, v. 14, p. 67-80. <https://doi.org/10.1016/j.quageo.2012.04.017>

595 Hua, Q., Turnbull, J. C., Santos, G. M., Rakowski, A. Z., Ancapichún, S., De Pol-Holz, R., Hammer, S.,
596 Lehman, S. J., Levin, I., Miller, J. B., Palmer, J. G., and Turney, C. S. M., 2021, Atmospheric
597 radiocarbon for the period 1950-2019: *Radiocarbon*, p. 1-23.
598 <https://doi.org/10.1017/RDC.2021.95>

599 Jamieson, R. A., Baldini, J. U. L., Frappier, A. B., and Müller, W., 2015, Volcanic ash fall events identified
600 using principal component analysis of a high-resolution speleothem trace element dataset:
601 *Earth and Planetary Science Letters*, v. 426, p. 36-45.
602 <https://doi.org/10.1016/j.epsl.2015.06.014>

603 Johnson, K., Hu, C., Belshaw, N., and Henderson, G., 2006, Seasonal trace-element and stable-isotope
604 variations in a Chinese speleothem: The potential for high-resolution paleomonsoon
605 reconstruction: *Earth and Planetary Science Letters*, v. 244, no. 1-2, p. 394-407.
606 <https://doi.org/10.1016/j.epsl.2006.01.064>

607 Kirch, P. V., 2000, On the road of the winds: an archaeological history of the Pacific Islands before the
608 European contact, Berkeley, California : University of California Press.

609 Li, H.-C., Ku, T.-L., You, C.-F., Cheng, H., Edwards, R. L., Ma, Z.-B., Tsai, W.-s., and Li, M.-D., 2005,
610 $^{87}\text{Sr}/^{86}\text{Sr}$ and Sr/Ca in speleothems for paleoclimate reconstruction in Central China between
611 70 and 280 kyr ago: *Geochimica et Cosmochimica Acta*, v. 69, no. 16, p. 3933-3947.
612 <https://doi.org/10.1016/j.gca.2005.01.009>

613 Markowska, M., Fohlmeister, J., Treble, P. C., Baker, A., Andersen, M. S., and Hua, Q., 2019, Modelling
614 the ^{14}C bomb-pulse in young speleothems using a soil carbon continuum model: *Geochimica*
615 *et Cosmochimica Acta*, v. 261, p. 342-367. <https://doi.org/10.1016/j.gca.2019.04.029>

616 Marshall, P., 1930, Geology of Rarotonga and Atiu, Bernice P. Bishop Museum Bulletin, v. 72.

617 Mathey, D., Lowry, D., Duffet, J., Fisher, R., Hodge, E., and Frisia, S., 2008, A 53 year seasonally resolved
618 oxygen and carbon isotope record from a modern Gibraltar speleothem: Reconstructed drip
619 water and relationship to local precipitation: *Earth and Planetary Science Letters*, v. 269, no.
620 1-2, p. 80-95. <https://doi.org/10.1016/j.epsl.2008.01.051>

621 Meteorology, A. B. o., and CSIRO, 2011, Climate Change in the Pacific: Scientific Assessment and New
622 Research. Volume 2. Country Reports.

623 Miorandi, R., Borsato, A., Frisia, S., Fairchild, I. J., and Richter, D. K., 2010, Epikarst hydrology and
624 implications for stalagmite capture of climate changes at Grotta di Ernesto (NE Italy): results
625 from long-term monitoring: *Hydrological Processes*, v. 24, no. 21, p. 3101-3114.
626 <https://doi.org/10.1002/hyp.7744>

627 Nagra, G., Treble, P. C., Andersen, M. S., Bajo, P., Hellstrom, J., and Baker, A., 2017, Dating stalagmites
628 in mediterranean climates using annual trace element cycles: *Sci Rep*, v. 7, no. 1, p. 621.
629 <https://doi.org/10.1038/s41598-017-00474-4>

630 Noronha, A. L., Johnson, K. R., Southon, J. R., Hu, C., Ruan, J., and McCabe-Glynn, S., 2015, Radiocarbon
631 evidence for decomposition of aged organic matter in the vadose zone as the main source of
632 speleothem carbon: *Quaternary Science Reviews*, v. 127, p. 37-47.
633 <https://doi.org/10.1016/j.quascirev.2015.05.021>

634 Oriani, F., Treble, P. C., Baker, A., and Mariethoz, G., 2022, WICount: Geological lamination detection
635 and counting using an image analysis approach: *Computers & Geosciences*, v. 160, p. 105037.
636 <https://doi.org/10.1016/j.cageo.2022.105037>

637 Orland, I. J., Burstyn, Y., Bar-Matthews, M., Kozdon, R., Ayalon, A., Matthews, A., and Valley, J. W.,
638 2014, Seasonal climate signals (1990–2008) in a modern Soreq Cave stalagmite as revealed by
639 high-resolution geochemical analysis: *Chemical Geology*, v. 363, p. 322-333.
640 <https://doi.org/10.1016/j.chemgeo.2013.11.011>

641 Paterson, D., de Jonge, M. D., Howard, D. L., Lewis, W., McKinlay, J., Starritt, A., Kusel, M., Ryan, C. G.,
642 Kirkham, R., Moorhead, G., Siddons, D. P., McNulty, I., Eyberger, C., and Lai, B., 2011, The X-

643 ray Fluorescence Microscopy Beamline at the Australian Synchrotron, p. 219-222.
644 <https://doi.org/10.1063/1.3625343>

645 Richards, D. A., Bottrell, S. H., Cliff, R. A., Ströhle, K., and Rowe, P. J., 1998, U-Pb dating of a speleothem
646 of Quaternary age: *Geochimica et Cosmochimica Acta*, v. 62, no. 23, p. 3683-3688.
647 [https://doi.org/10.1016/S0016-7037\(98\)00256-7](https://doi.org/10.1016/S0016-7037(98)00256-7)

648 Ryan, C. G., Kirkham, R., Siddons, D. P., Dunn, P. A., Laird, J. S., Kuczewski, A., Moorhead, G., De
649 Geronimo, G., Davey, P., Jensen, M., Paterson, D. J., de Jonge, M. D., Howard, D. L., and Hough,
650 R. M., 2010, The Maia 384 detector array in a nuclear microprobe: A platform for high
651 definition PIXE elemental imaging: *Nuclear Instruments and Methods in Physics Research*
652 *Section B: Beam Interactions with Materials and Atoms*, v. 268, no. 11, p. 1899-1902.
653 <https://doi.org/10.1016/j.nimb.2010.02.052>

654 Scholz, D., and Hoffmann, D., 2008, 230Th/U-dating of fossil corals and speleothems: *E&G –*
655 *Quaternary Science Journal*, v. 57, no. 1-2. <http://doi.org/10.23689/fidgeo-1056>

656 Scroxton, N., Walczak, M., Markowska, M., Zhao, J.-x., and Fallon, S., 2021, Historical droughts in
657 Southeast Australia recorded in a New South Wales stalagmite: *The Holocene*, v. 31, no. 4, p.
658 607-617. <https://doi.org/10.1177/0959683620981717>

659 Stoddart, D. R., Woodroffe, C., and Spencer, T., 1990, Mauke, Mitiaro and Atiu: Geomorphology of
660 makatea islands in the southern Cooks. <https://doi.org/10.5479/si.00775630.341.1>

661 Stuiver, M., and Polach, H. A., 1977, Discussion Reporting of 14C Data: *Radiocarbon*, v. 19, no. 3, p.
662 355-363. <https://doi.org/10.1017/S0033822200003672>

663 Sundqvist, H. S., Holmgren, K., Fohlmeister, J., Zhang, Q., Matthews, M. B., Spötl, C., and Körnich, H.,
664 2013, Evidence of a large cooling between 1690 and 1740 AD in southern Africa: *Scientific*
665 *Reports*, v. 3, no. 1, p. 1767. <https://doi.org/10.1038/srep01767>

666 Tan, M., Baker, A., Genty, D., Smith, C., Esper, J., and Cai, B., 2006, Applications of stalagmite laminae
667 to paleoclimate reconstructions: Comparison with dendrochronology/climatology:
668 *Quaternary Science Reviews*, v. 25, no. 17, p. 2103-2117.
669 <https://doi.org/10.1016/j.quascirev.2006.01.034>

670 Treble, P., Shelley, J. M. G., and Chappell, J., 2003, Comparison of high resolution sub-annual records
671 of trace elements in a modern (1911–1992) speleothem with instrumental climate data from
672 southwest Australia: *Earth and Planetary Science Letters*, v. 216, no. 1-2, p. 141-153.
673 [https://doi.org/10.1016/s0012-821x\(03\)00504-1](https://doi.org/10.1016/s0012-821x(03)00504-1)

674 Treble, P. C., Chappell, J., Gagan, M. K., McKeegan, K. D., and Harrison, T. M., 2005, In situ
675 measurement of seasonal $\delta^{18}\text{O}$ variations and analysis of isotopic trends in a modern
676 speleothem from southwest Australia: *Earth and Planetary Science Letters*, v. 233, no. 1, p.
677 17-32. <https://doi.org/10.1016/j.epsl.2005.02.013>

678 Trotter, M. M., and Duff, R., 1974, Prehistory of the Southern Cook Islands, Canterbury Museum Trust
679 Board.

680 Vansteenberge, S., de Winter, N. J., Sinnesael, M., Verheyden, S., Goderis, S., Van Malderen, S. J. M.,
681 Vanhaecke, F., and Claeys, P., 2020, Reconstructing seasonality through stable-isotope and
682 trace-element analyses of the Proserpine stalagmite, Han-sur-Lesse cave, Belgium: indications
683 for climate-driven changes during the last 400 years: *Clim. Past*, v. 16, no. 1, p. 141-160.
684 <https://doi.org/10.5194/cp-16-141-2020>

685 Wang, J. K., Johnson, K. R., Borsato, A., Amaya, D. J., Griffiths, M. L., Henderson, G. M., Frisia, S., and
686 Mason, A., 2019, Hydroclimatic variability in Southeast Asia over the past two millennia: *Earth*
687 *and Planetary Science Letters*, v. 525, p. 115737. <https://doi.org/10.1016/j.epsl.2019.115737>

688 Weir, T., Kumar, R., and Ngari, A., 2021, Interdecadal modulation of the effect of ENSO on rainfall in
689 the southwestern Pacific: *Journal of Southern Hemisphere Earth Systems Science*, v. 71, no. 1,
690 p. 53-65. <https://doi.org/10.1071/ES19053>

691 Widlansky, M. J., Timmermann, A., Stein, K., McGregor, S., Schneider, N., England, M. H., Lengaigne,
692 M., and Cai, W., 2012, Changes in South Pacific rainfall bands in a warming climate: *Nature*
693 *Climate Change*, v. 3, p. 417. <https://doi.org/10.1038/nclimate1726>

694 Xie, S.-P., Deser, C., Vecchi, G. A., Ma, J., Teng, H., and Wittenberg, A. T., 2010, Global Warming Pattern
695 Formation: Sea Surface Temperature and Rainfall: *Journal of Climate*, v. 23, no. 4, p. 966-986.
696 <https://doi.org/10.1175/2009jcli3329.1>
697 Zhao, J.-x., Wang, Y.-j., Collerson, K. D., and Gagan, M. K., 2003, Speleothem U-series dating of semi-
698 synchronous climate oscillations during the last deglaciation: *Earth and Planetary Science*
699 *Letters*, v. 216, no. 1, p. 155-161. [https://doi.org/10.1016/S0012-821X\(03\)00501-6](https://doi.org/10.1016/S0012-821X(03)00501-6)

700